

Direct numerical simulation of supersonic turbulent boundary layer subjected to a curved compression ramp

Fulin Tong, Xinliang Li, Yanhui Duan, and Changping Yu

Citation: *Physics of Fluids* **29**, 125101 (2017);

View online: <https://doi.org/10.1063/1.4996762>

View Table of Contents: <http://aip.scitation.org/toc/phf/29/12>

Published by the *American Institute of Physics*

Articles you may be interested in

[The culmination of an inverse cascade: Mean flow and fluctuations](#)

Physics of Fluids **29**, 125102 (2017); 10.1063/1.4985998

[On the convergence and scaling of high-order statistical moments in turbulent pipe flow using direct numerical simulations](#)

Physics of Fluids **29**, 125105 (2017); 10.1063/1.4996882

[Development of vortex structures in the wake of a sharp-edged bluff body](#)

Physics of Fluids **29**, 125103 (2017); 10.1063/1.5003114

[From two-dimensional to three-dimensional turbulence through two-dimensional three-component flows](#)

Physics of Fluids **29**, 111101 (2017); 10.1063/1.4990082

[Symmetric/asymmetric separation transition in a supersonic combustor with single-side expansion](#)

Physics of Fluids **29**, 126102 (2017); 10.1063/1.4990668

[Flapping foil power generator performance enhanced with a spring-connected tail](#)

Physics of Fluids **29**, 123601 (2017); 10.1063/1.4998202



**COMPLETELY
REDESIGNED!**

Physics Today Buyer's Guide
Search with a purpose.

Direct numerical simulation of supersonic turbulent boundary layer subjected to a curved compression ramp

Fulin Tong,^{1,2} Xinliang Li,^{2,3} Yanhui Duan,¹ and Changping Yu^{2,a)}

¹Computational Aerodynamics Institute of China Aerodynamics Research and Development Center, Mianyang 621000, China

²LHD, Institute of Mechanics, Chinese Academy of Sciences, Beijing 100190, China

³School of Engineering Science, University of Chinese Academy of Sciences, Beijing 100049, China

(Received 18 July 2017; accepted 9 November 2017; published online 11 December 2017)

Numerical investigations on a supersonic turbulent boundary layer over a longitudinal curved compression ramp are conducted using direct numerical simulation for a free stream Mach number $M_\infty = 2.9$ and Reynolds number $Re_\theta = 2300$. The total turning angle is 24° , and the concave curvature radius is 15 times the thickness of the incoming turbulent boundary layer. Under the selected conditions, the shock foot is transferred to a fan of the compression wave because of the weaker adverse pressure gradient. The time-averaged flow-field in the curved ramp is statistically attached where the instantaneous flow-field is close to the intermittent transitory detachment state. Studies on coherent vortex structures have shown that large-scale vortex packets are enhanced significantly when the concave curvature is aligned in the spanwise direction. Consistent with findings of previous experiments, the effect of the concave curvature on the logarithmic region of the mean velocity profiles is found to be small. The intensity of the turbulent fluctuations is amplified across the curved ramp. Based on the analysis of the Reynolds stress anisotropy tensor, the evolutions of the turbulence state in the inner and outer layers of the boundary layer are considerably different. The curvature effect on the transport mechanism of the turbulent kinetic energy is studied using the balance analysis of the contributing terms in the transport equation. Furthermore, the Görtler instability in the curved ramp is quantitatively analyzed using a stability criterion. The instantaneous streamwise vorticity confirms the existence of the Görtler-like structures. These structures are characterized by an unsteady motion. In addition, the dynamic mode decomposition analysis of the instantaneous flow field at the spanwise/wall-normal plane reveals that four dynamical relevant modes with performance loss of 16% provide an optimal low-order representation of the essential characteristics of the numerical data. The spatial structures of the dominated low-frequency dynamic modes are found to be similar to that of the Görtler-like vortices. *Published by AIP Publishing.* <https://doi.org/10.1063/1.4996762>

I. INTRODUCTION

The supersonic turbulent boundary layer subjected to a concave curvature is a benchmark flow phenomenon in practice, which is dominated by the combined effect of complex physical mechanisms, such as the longitudinal curvature,¹ pressure gradient,² and the associated additional strain rates induced by bulk compression and dilatation.³ In contrast to the stability of the convex curvature, the concave curvature destabilizes and exhibits a reinforcing effect on the turbulence level. Another significant flow characteristic is the centrifugal instability, which may induce Taylor-Görtler type^{4,5} vortices associated with large spanwise variations in the skin friction. Because of the strong nonlinear interaction in the curved region, the concave effect on the turbulence structure has not been fully understood and is significant for improving the understanding of the relevant mechanisms of this complicated flow.

Many researchers have investigated the behavior of a supersonic turbulent boundary layer along a concave curvature. Most early experiments focused on the mean velocity scaling.^{6,7} Similar to the results obtained for a flat plate with an adverse pressure gradient, the mean velocity profiles in the curved region exhibited an increase trend in the wake region and a dip below the logarithmic law in the outer edge of the inner layer. To analyze the curvature radius effect on the turbulence behavior, Jayaram *et al.*⁶ studied a supersonic turbulent boundary layer subjected to a concave surface curvature with two different radii, i.e., 10 and 50 times the thickness of the upstream boundary layer. In their experiments, the total perturbation level in both cases of the radii was the same because the turning angle was kept constant; however, the perturbation rate changed dramatically because of the different curvature radii. They found that the total strain affected the shorter radius mode, exhibiting a marked increase in the Reynolds stress ratio and the length and time scale of the turbulent motions. However, the longer radius mode was sensitive to the local strain, and the structural parameters remained unchanged.

^{a)} Author to whom correspondence should be addressed: cpyu@imech.ac.cn

Donovan *et al.*⁷ experimentally investigated the changes in the instantaneous structure of a supersonic turbulent boundary layer that developed along a concave surface with a turning angle of 16°. As evidenced by the large gradient in the fluctuating stream mass flux, the significant change in the large-scale organization in the boundary layer was verified. Recently, Wang *et al.*^{8,9} experimentally investigated the coherent vortex structure of a supersonic concave turbulent boundary layer with a turning angle of 20°. They found that the concave curvature exhibited a reinforcing effect on the large-scale hairpin packets. Concave curvatures are generally sensitive to longitudinal vortices. Hoffmann *et al.*¹⁰ studied the effect of a concave curvature on an incompressible boundary layer and showed that the longitudinal vortices were indirectly responsible for inducing significant changes in the turbulent structure. In contrast to that observed in a subsonic boundary layer, Sturek and Danberg¹¹ and Laderman¹² did not find any evidence of steady Taylor-Görtler type vortices in supersonic concave-curved flows. They suggested that the formation of longitudinal roll cells could be prevented via the nonlinear interaction between the concave curvature and the compression ramp. However, Jayaram *et al.*⁶ concluded that the measurement techniques employed were unsuitable for detecting Taylor-Görtler type vortices, which might be characteristic of an unsteady motion.

Although the response of a supersonic turbulent boundary layer subjected to a concave curvature has been experimentally studied, high-fidelity numerical calculations are limited. In recent years, direct numerical simulation (DNS) and large eddy simulation (LES) have been developed for compressible wall-bounded flows with significant success.^{13–17} However, to the best of the author's knowledge, only a few DNS analyses have been conducted on a supersonic turbulent boundary layer subjected to a curved compression ramp.

Hence, in this study, the compressible turbulent boundary layer over a curved compression ramp for a free-stream Mach number $M_\infty = 2.9$ and a Reynolds number $Re_0 = 2300$ was numerically investigated. The inflow conditions are the same with the previous numerical analysis of a separated 24° compression ramp.¹⁸ The three-dimensional compressible Navier-Stokes equations were solved using the DNS with the help of a modified weighted essentially non-oscillatory (WENO) scheme and a limiter technique.¹⁷ The motivation of this study is to improve the basic understanding of the supersonic curved flow by thoroughly analyzing the DNS data.

II. COMPUTATIONAL SETUP

A. Governing equations

The governing equations are the non-dimensionalized conservative forms of the continuity, momentum, and energy equations in curvilinear coordinates. The equations are non-dimensionalized by the inflow parameters. The unit of the reference length is millimeters,

$$\frac{\partial U}{\partial t} + \frac{\partial F}{\partial \xi} + \frac{\partial G}{\partial \eta} + \frac{\partial H}{\partial \zeta} = 0, \quad (1)$$

where

$$U = J \begin{Bmatrix} \rho \\ \rho u \\ \rho v \\ \rho w \\ \rho e \end{Bmatrix} \text{ and } F = F_c + F_v = Jr_\xi \begin{Bmatrix} \rho u^* \\ \rho u u^* + p s_x \\ \rho v u^* + p s_y \\ \rho w u^* + p s_z \\ (\rho e + p) u^* \end{Bmatrix} - Jr_\xi \begin{Bmatrix} 0 \\ \sigma_{xx} s_x + \sigma_{xy} s_y + \sigma_{xz} s_z \\ \sigma_{yx} s_x + \sigma_{yy} s_y + \sigma_{yz} s_z \\ \sigma_{zx} s_x + \sigma_{zy} s_y + \sigma_{zz} s_z \\ \tau_x s_x + \tau_y s_y + \tau_z s_z \end{Bmatrix}, \quad (2)$$

where

$$s_x = \xi_x / r_\xi, \quad u^* = u s_x + v s_y + w s_z, \quad r_\xi = \sqrt{\xi_x^2 + \xi_y^2 + \xi_z^2}, \\ \tau_x = \sigma_{xx} u + \sigma_{xy} v + \sigma_{xz} w - q_x, \quad (3) \\ \tau_y = \sigma_{yx} u + \sigma_{yy} v + \sigma_{yz} w - q_y, \\ \tau_z = \sigma_{zx} u + \sigma_{zy} v + \sigma_{zz} w - q_z.$$

Here, F_c and F_v denote the convective and viscous terms, respectively. The flux terms G and H have similar forms as F . The viscous stress and heat flux terms are obtained from the following Newtonian and Fourier models:

$$\sigma_{ij} = \frac{2\mu}{\text{Re}} \left[\frac{1}{2} \left(\frac{\partial u_i}{\partial x_j} + \frac{\partial u_j}{\partial x_i} \right) - \frac{1}{3} \frac{\partial u_k}{\partial x_k} \delta_{ij} \right]$$

and

$$q_j = -\frac{\mu}{(\gamma - 1) \text{Re} \text{Pr} M_\infty^2} \frac{\partial T}{\partial x_j}. \quad (4)$$

Here, the temperature dependence of μ is based on the Sutherland's law, and the relationship between the thermodynamic variables is given by the ideal gas law,

$$\mu(T) = T^{3/2} (1 + 0.82) / (T + 0.82) \text{ and } p = \frac{\rho T}{\gamma M_\infty^2}. \quad (5)$$

B. Numerical methods

When a supersonic turbulent boundary layer develops along a curved compression ramp, the complicated flow is characterized by the interaction between the shock wave and the turbulent boundary layer. The previous DNS of the compressible turbulent boundary layer shows that the numerical dissipation in the numerical method should be kept minimum to resolve the small-scale turbulence structure. However, to avoid spurious oscillation in the shock region, an appropriate dissipative scheme must be selected. The WENO method is one of the suitable schemes whereby the conflicting objectives can be met. Previous studies^{17,19} on the WENO method have shown that the dissipation in smooth region is still relatively high. To solve this problem, the WENO methods have been modified and applied successfully to the simulation of shock-turbulence interaction dominated complex flows.

In this simulation, the convective terms in Eqs. (1) and (2) are computed using a dissipation-optimized WENO method,

which is proposed by Martin *et al.*²⁰ Owing to the symmetry of the candidate stencil used, the order of accuracy and bandwidth resolution are optimized, while minimizing the dissipation. More details about this method can be found elsewhere.²⁰ Wu and Martin¹⁷ have demonstrated that the numerical dissipation can be further reduced using a relatively linear method defined as follows:

$$\omega_k = \begin{cases} C_k, & \text{if } TV_{\max}/TV_{\min} < A_{RL}^{TV} \text{ and } TV_{\max} < B_{RL}^{TV} \\ \omega_k, & \text{otherwise} \end{cases} \quad (6)$$

Here, ω_k denotes the weights and C_k denotes the optimal weights.²⁰ TV_{\max} and TV_{\min} denote the maximum and minimum total variation of each candidate stencil, respectively. The threshold values A_{RL}^{TV} and B_{RL}^{TV} are used to stabilize the simulation. In addition, the viscous terms are computed using an eighth-order central scheme, and the time integration is performed using the third-order total-variation-diminishing (TVD) Runge–Kutta method.²¹

C. Computational domain and boundary conditions

Figure 1(a) shows the computational domain, including the upstream flat plate and the curved compression ramp. In this simulation, the streamwise domain ranges from $x = -335$ mm to $x = 55$ mm. The length of the flat plate is crucial to the generation of the inflow turbulent boundary layer, which is introduced later in this paper. The turning angle of the curved ramp is 24° , and the curvature radius is 97.5 mm, corresponding to approximately 15δ . Unless otherwise stated in this paper, δ denotes the turbulent boundary layer thickness at the

reference location, indicated in Fig. 1. The curved region exists in the range -20 mm $< x < 20$ mm. The normal extent of the computational domain is 35 mm. In the previous DNS of compression ramps,^{16,17} the size of the spanwise domain was generally two times the thickness of the incoming boundary layer. However, to eliminate any spurious dynamics and to determine the large-scale Görtler vortex, the spanwise size of the computational domain in the present simulation extends up to 7.5δ .

The computational mesh is generated algebraically with $2500 \times 160 \times 480$ nodes in the streamwise, wall-normal, and spanwise directions, respectively. As shown in Fig. 1(b), the grid points are equally spaced in the curved compression ramp and stretched in the sponge region downstream. The grid points in the wall-normal direction are clustered in the near-wall region, ensuring approximately 100 points inside the boundary layer. The grids in the spanwise direction are uniformly spaced. In the wall units based on the viscous length scale, which is defined as $\mu_w/(\rho_w u_\tau)$ at the reference location, the grid resolutions in the curved region are $\Delta x^+ \approx 4.5$, $\Delta y_w^+ \approx 0.5$, and $\Delta z^+ \approx 5.0$, which are comparable with those obtained in the DNS of previous compression ramps.¹⁷

The generation of the inflow turbulent boundary layer²² is a critical issue in the simulation of the curved flow. In this study, a fully developed incoming turbulent boundary layer is obtained via the laminar-to-turbulent transition within the upstream flat plate. First, the profile of the compressible laminar boundary layer is enforced at the inlet of the computational domain, and subsequently, a region of blowing and suction disturbance,²³ shown in Fig. 1, is introduced to induce the transition to turbulence. More details about the disturbance can be found elsewhere.²³ To ensure that the turbulence at the reference location attains an equilibrium state, the length of the flat plate must be sufficient. Table I lists the parameters of the boundary layer at the reference location, where δ , δ^* , θ , and C_f denote the thickness, displaced thickness, momentum thickness, and wall skin-friction coefficient, respectively. Evidently, the statistical quantities of the boundary layer at the reference location are in good agreement with the DNS results obtained by Wu and Martin¹⁷ and the experimental data presented by Bookey *et al.*¹⁸

In addition, a no-slip and adiabatic wall condition is applied to the ramp surface. To avoid the reflection of the numerical disturbance, a buffer region^{14,15} with progressively coarsening meshes is assumed near the far field and outlet boundary. Periodic boundary conditions are used in the spanwise direction of the computational domain.

TABLE I. Parameters of the turbulent boundary layer at the reference location.

Case	δ (mm)	δ^* (mm)	θ (mm)	C_f
Current DNS	6.5	2.06	0.41	0.00256
Wu and Martin ¹⁷	6.7	2.36	0.43	0.00225
Bookey <i>et al.</i> ¹⁸	6.4	1.80	0.38	0.00217

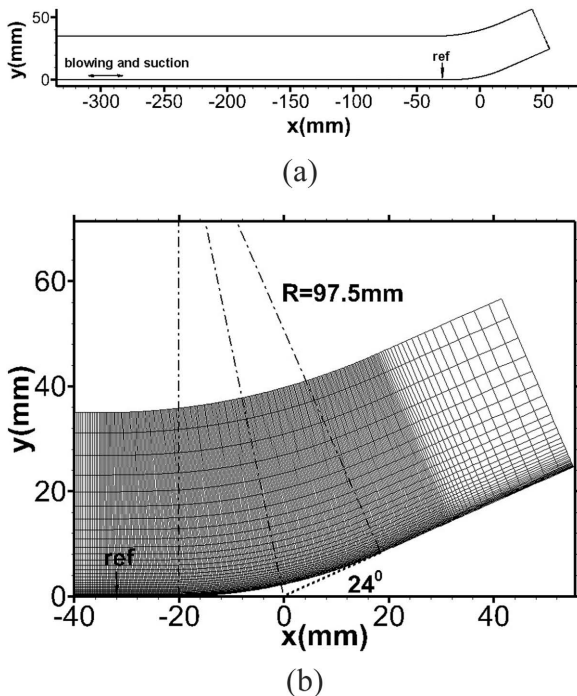


FIG. 1. (a) Sketch of the computational domain and (b) the grid points in the curved compression ramp. The grid is plotted at intervals of five points in both the x and y directions.

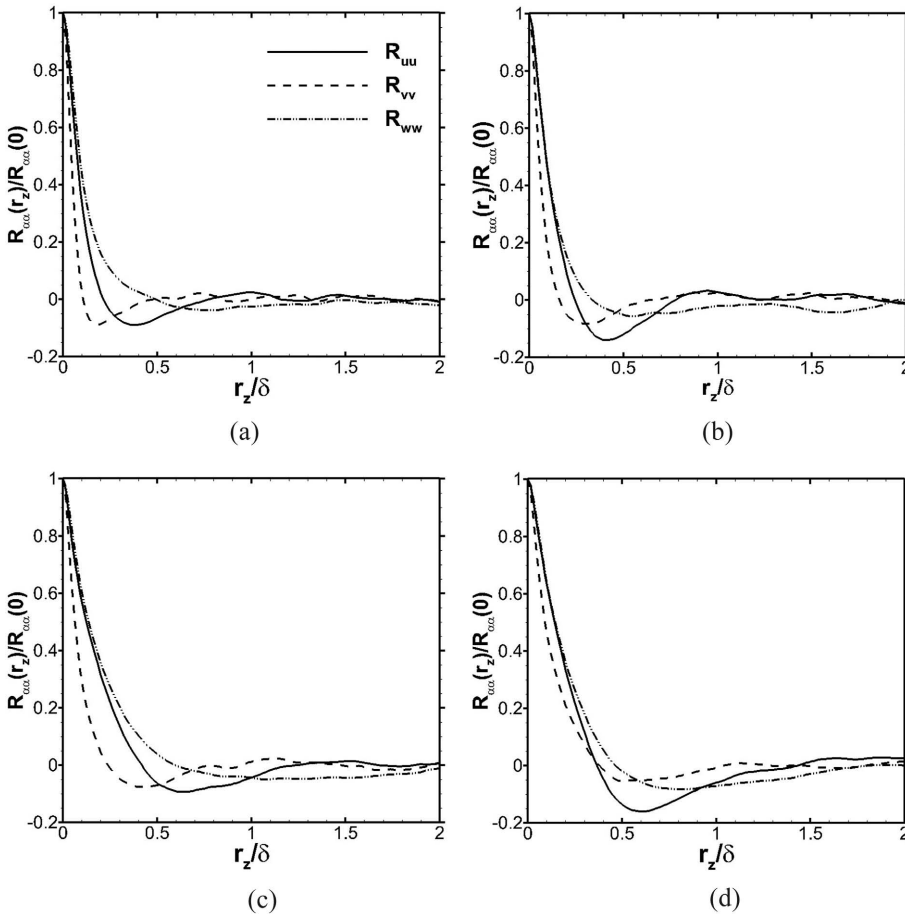


FIG. 2. Two-point correlation coefficient of the velocity at various locations: (a) $x = -35$ mm and $y^+ = 50$, (b) $x = 0$ mm and $y^+ = 50$, (c) $x = 30$ mm and $y^+ = 50$, and (d) $x = 30$ mm and $y/\delta = 0.5$.

To assess the validity of the computational domain, Fig. 2 shows the two-point correlation coefficient as a function of the spanwise distance, which is defined as $R_{\alpha\alpha}(K_r \Delta z) = \frac{1}{N_z - 1} \sum_{k=1}^{N_z-1} \langle \alpha_K \alpha_{K+K_r} \rangle$, $K_r = 0, 1, \dots, N_z - 1$. Here, α represents the fluctuations of the flow field. The streamwise locations are selected at $x = -35$ mm and $x = 0$ mm, corresponding to the upstream boundary layer and the curved region, respectively. As shown in Fig. 2, the correlation coefficient at both locations rapidly tends to zero with the increase in the spanwise distance. It is clear that the change in the correlation coefficient is negligible when the distance is beyond 2.0δ , suggesting that the spanwise domain in this simulation is sufficiently wide to resolve the turbulence dynamics.

III. RESULTS AND DISCUSSIONS

A. Incoming turbulent boundary layer

The generation of a realistic incoming turbulent boundary layer plays a key role in the following simulation. Figure 3 shows the instantaneous density gradient in the upstream flat-plate boundary layer. The entire transition process to a turbulence flow induced by the wall blowing and suction is clearly revealed. As shown in Fig. 3, the outer region of the boundary layer at $x > -50$ mm is characterized by

large-scale bulges, indicating the appearance of a fully developed turbulent boundary layer.

Using the mean and fluctuation quantities, the statistical characteristics of the fully developed turbulent boundary layer are quantitatively verified with the empirical correlations and previous numerical results. Figure 4 shows the van Driest transformed mean velocity profile at the reference locations based on the current DNS data. In this paper, the variable y^* denotes the wall normal distance in the curvilinear

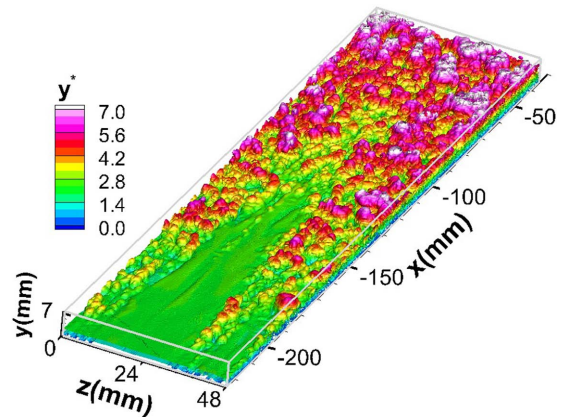


FIG. 3. Isosurface of the instantaneous density gradient colored by the wall-normal distance (y^*) in the upstream flat-plate boundary layer.

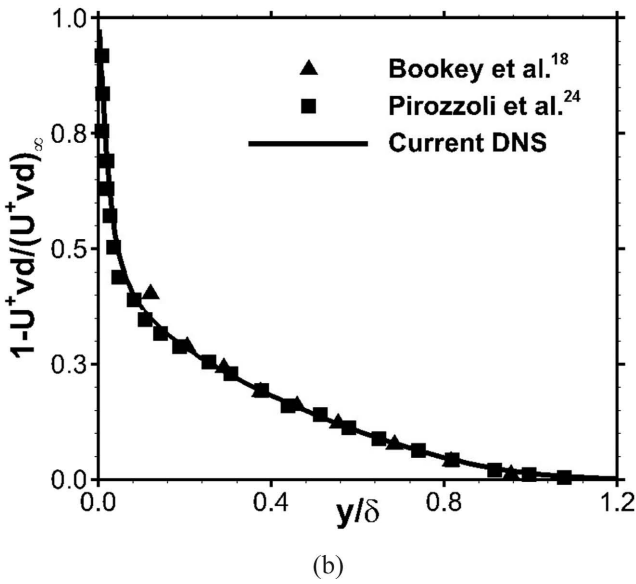
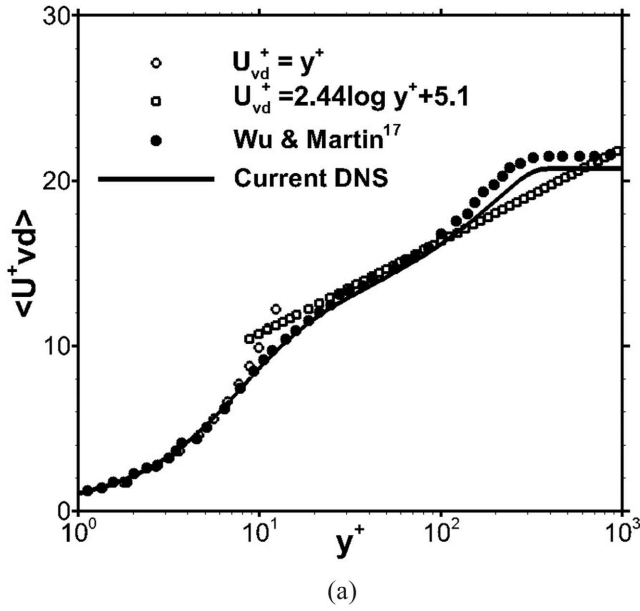


FIG. 4. (a) van Driest transformed mean velocity profile in the inner scaling and (b) van Driest transformed mean deficit velocity profile in the outer scaling. The results are taken at the reference location.

coordinates. The variable u^+ represents the transformed velocity, which is defined as $u^+ = \frac{u}{u_\tau} \sqrt{Re}$, $u_\tau = \sqrt{\frac{\tau_w}{\rho_w}}$. The variable y^+ represents the wall-normal coordinate, which is renormalized by $y^+ = y \frac{\rho_w u_\tau}{\mu} \sqrt{Re}$. The profile exhibits a linear behavior in the sub-layer for $y^+ < 6$, and the logarithmic region is consistent with the logarithmic scaling for $30 < y^+ < 60$. In addition, the recent DNS results are in good agreement with the experimental and previous DNS data.^{17,18,24} Figure 5 shows the turbulent fluctuation intensity of the three velocity components in the inner and outer scaling, respectively. Based on the Morkovin's hypothesis, the turbulent fluctuation is scaled using the density. The current DNS data are in good agreement with the well-established incompressible DNS data^{25,27} and experimental measurements.²⁶ For instance, the streamwise velocity fluctuation, shown in Fig. 5(a), attains a peak value of

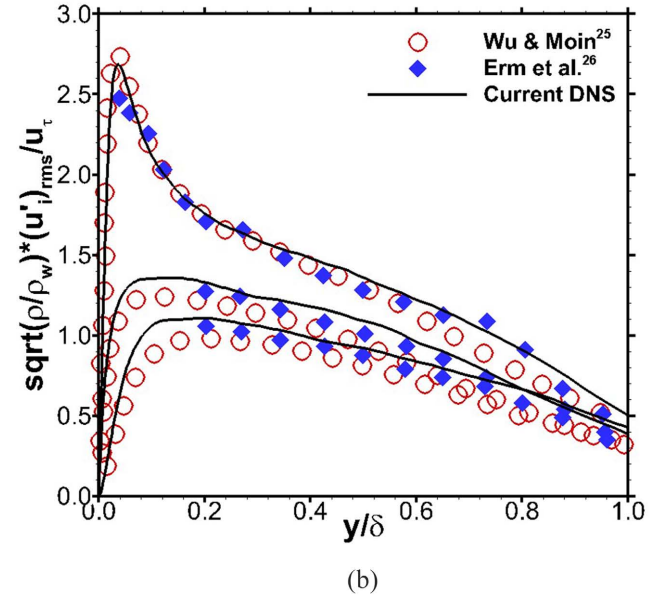
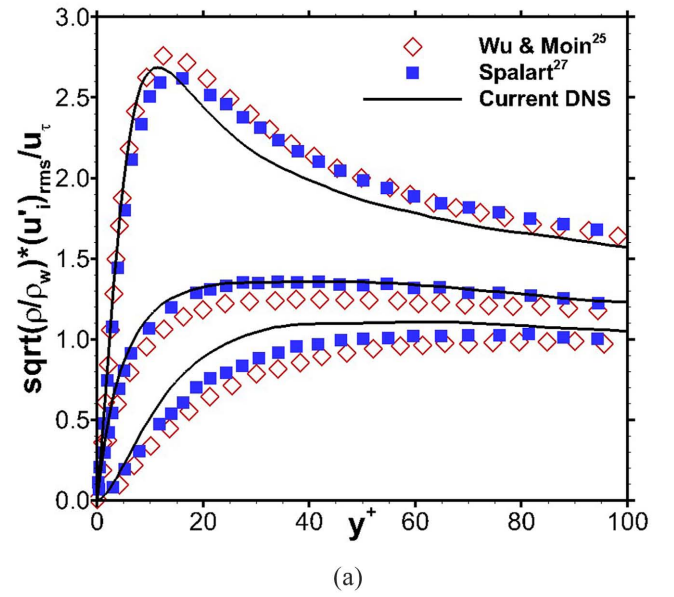


FIG. 5. Profiles of the turbulence fluctuation taken at the reference location in the (a) inner scaling and (b) outer scaling.

2.68 at $y^+ = 11$, which is comparable to that of incompressible flows.^{25,27}

B. Instantaneous and mean flow fields

Figure 6 shows the numerical schlieren of the instantaneous flow field in the streamwise/wall-normal plane, in which the parameter is defined as $0.8 \exp[-10(|\nabla \rho| - |\nabla \rho|_{\min})/(|\nabla \rho|_{\max} - |\nabla \rho|_{\min})]$. It is clear that the shock wave penetrates into the boundary layer and gradually evolves as a fan of the compressive wave. The high values of the density gradient are indicated by the dark regions. We can observe qualitatively that the intensity of the turbulence fluctuations downstream of the curved ramp is amplified as the flow develops. Figure 7 shows the coherent vortex structures obtained using the Q criterion.²⁸ In the incoming boundary layer, the near-wall region is dominated by elongated streamwise vortex

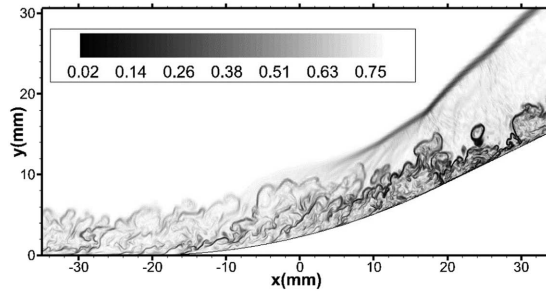


FIG. 6. Numerical visualization of the instantaneous flow field in the stream-wise and wall-normal plane.

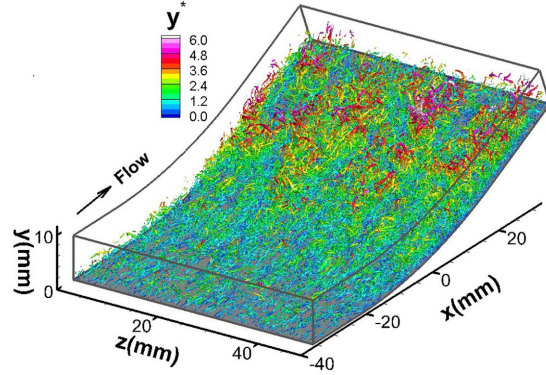


FIG. 7. Isosurface of the Q criterion colored by the wall normal distance (y^*).

structures. However, in the concave region, the structures are characterized by large-scale hairpin-like vortices in the outer region of the boundary layer. Moreover, another interesting scenario is that these vortices are concentrated as packets in the spanwise direction, exhibiting a trend similar to that of the Görtler-like vortices.

Figure 8 shows the streamwise distribution of the mean wall pressure in the curved ramp. There are no similar numerical and experimental data to validate the current DNS data. An auxiliary DNS of the compression ramp with the same inflow conditions and computational grid is performed in this study to verify the accuracy of the DNS results of the curved 24° ramp. The results show that the distribution of the wall pressure in the compression ramp is in good quantitative agreement with that of the DNS performed by Wu and Martin¹⁷ and

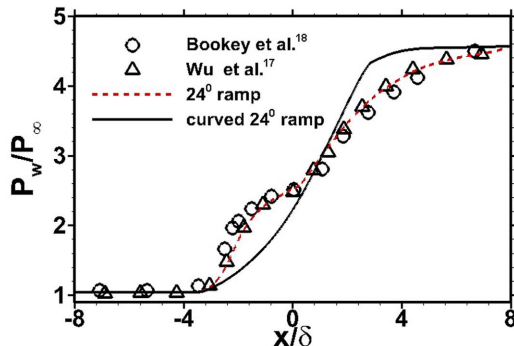


FIG. 8. Comparison of the mean wall pressure with the DNS and experimental data.

the experimental measurements performed by Bookey *et al.*¹⁸ A plateau of pressure in the corner region is obtained, indicating the separation of the mean flow field. However, the curved ramp results show no sign of a pressure plateau in the concave curvature because of the relatively weaker adverse gradient of the wall pressure.

Figure 9(a) shows the streamwise distribution of the mean and instantaneous wall skin-friction coefficients, where the theoretical value²⁹ obtained using the Blasius formulation with the van Driest II transformation is presented. Here, the mean and instantaneous results are both spanwise-averaged. Before the points at approximately $x = -30$ mm, the skin friction in the upstream flat-plate boundary layer shows a good agreement with the estimate, further supporting the above conclusions that the incoming turbulent boundary layer attains an equilibrium state. In the curved region, as expected, it is found that the skin friction decreases as the flow develops along the concave wall, followed by a slow increase in the downstream region of the curved ramp. However, in contrast to the flow reversal of the 24° compression ramp, the mean flow field in the curved ramp is attached statistically. Furthermore, the two instantaneous results, shown in Fig. 9(a), are considerably different. It is apparent that the former is separated instantaneously where the flow is attached at another instantaneous time. This is because of the weak adverse gradient induced by the concave curvature. To further demonstrate the intermittency of the flow separation, the contours of the instantaneous skin friction are plotted, as shown in Fig. 9(b). The negative skin frictions are indicated by contours marked in red. The scattered red spots are clearly visible in the curved region for -20 mm $< x < 20$ mm.

For a separated flow, Simpson³⁰ proposed a quantitative definition to classify the detachment state near the wall. In this study, following Simpson,³⁰ the detachment state is defined

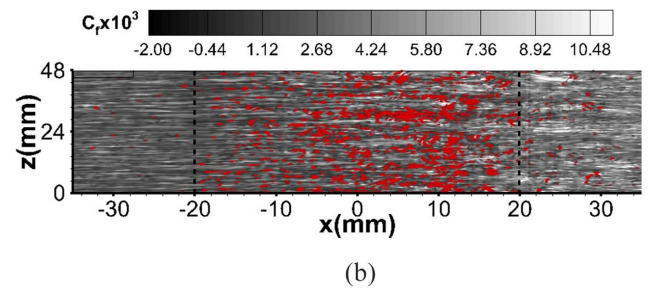
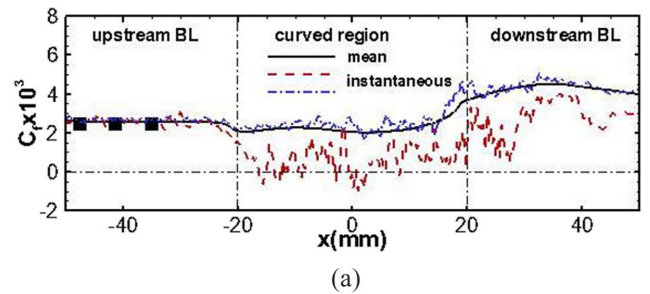


FIG. 9. (a) Streamwise distribution of the mean and instantaneous wall skin-friction coefficients and (b) contours of the instantaneous skin friction coefficient. The symbols denote the Blasius estimation. The negative value is denoted by red contours.

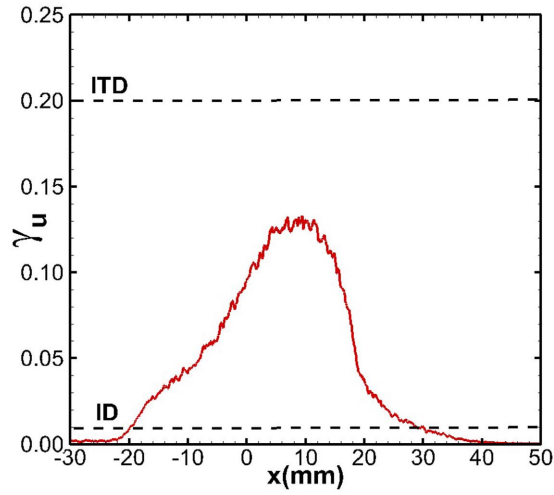


FIG. 10. Distribution of the statistical probability (γ_u) as a function of the streamwise location.

by the statistical probability on the basis of the friction time of that the instantaneous flow is separated. According to Simpson,³⁰ the instantaneous backflow of 1% of the total time is defined as the incipient detachment (ID) and intermittent transitory detachment (ITD) corresponding to an instantaneous backflow of 20% of the total time. If the probability of separation is over 50%, it is defined as a transitory detachment (TD). To quantitatively analyze the instantaneous separation in this simulation, Fig. 10 shows the streamwise distribution of the statistical probability (γ_u). It is apparent that the value in the incoming boundary layer and the downstream region of the concave wall is significantly smaller and within the range of the ID. Furthermore, the figure shows that the flow in the vicinity of the curved ramp is close to the ITD state in the curved region wherein γ_u varies between 0.01 and 0.14.

C. Turbulent boundary layer characteristics

To better analyze the evolution of the turbulent boundary layer throughout the curved compression ramp, the flow

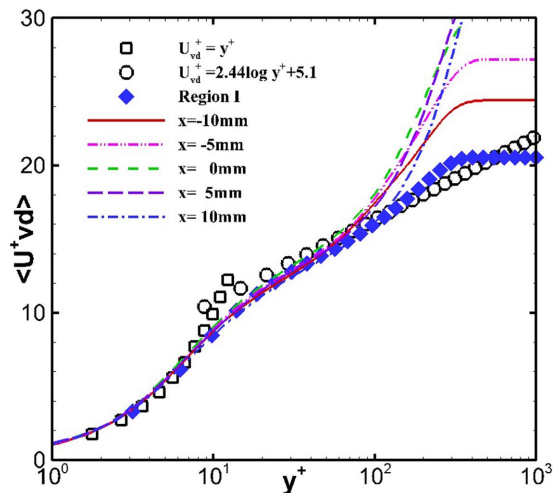
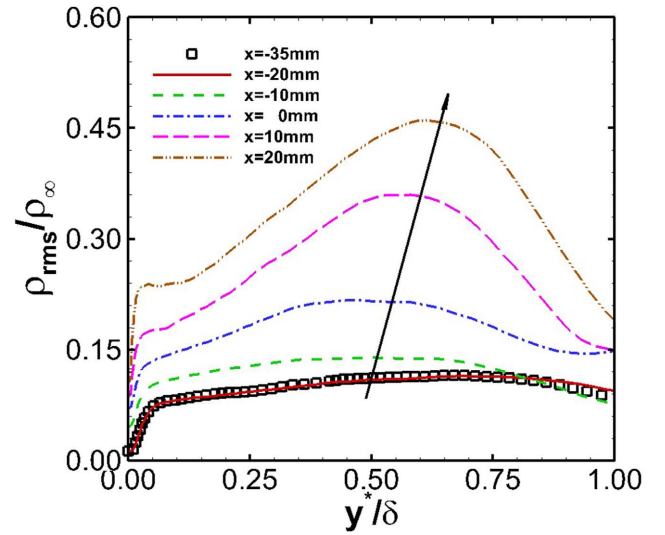


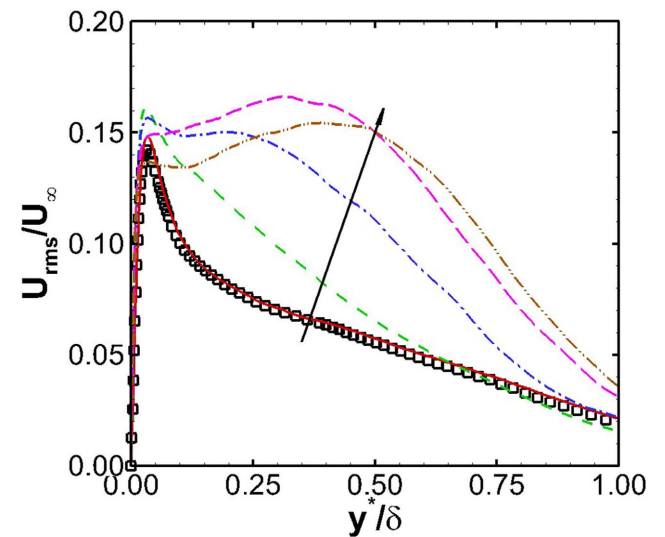
FIG. 11. Profiles of the van Driest transformed mean streamwise velocity in region II.

is divided into three regions: an upstream turbulent boundary layer (region I), the interaction region of the curved ramp (region II), and the downstream of the curved ramp (region III). Figure 9(a) shows the schematics of the corresponding streamwise locations of the regions. The curved region lies from $x = -20$ mm to $x = 20$ mm.

Figure 11 shows the profiles of the van Driest transformed mean streamwise velocity U^+_{vd} at selected locations in region II as a function of the wall-normal distance in wall units y^+ . For comparison, the data in region I, denoted by blue symbols, are included in this figure. As shown in Fig. 11, the velocity in region I is linear ($U^+_{vd} = y^+$) in the viscous sub-layer and obeys the logarithmic law ($U^+_{vd} = 2.44 \log y^+ + 5.1$) for $30 \leq y^+ \leq 100$. In the interaction region of compression ramp, the velocity profiles are characteristic of dips in the logarithmic region. The simulation of the curved ramp



(a)



(b)

FIG. 12. Wall-normal distribution of the density and velocity fluctuations at several streamwise locations: (a) density fluctuations and (b) streamwise velocity fluctuations.

indicates that the profiles in region II exhibit no obvious dips and the log-law is still preserved. This phenomenon is similar to the results of an experiment conducted using a turbulent boundary with a Mach number of 2.95 subjected to a concave surface curvature.^{8,9} Additionally, it is clear that the concave curvature affects the velocity profile in the wake region for $y^+ \geq 200$.

Figure 12 shows the wall-normal distribution of the density and streamwise velocity fluctuations at several streamwise locations. Clearly, the density and velocity fluctuations increase dramatically as the flow develops along the curved ramp. However, as shown in Fig. 12, the streamwise evolution processes of the density and velocity fluctuations are substantially different in the interaction regions. With respect

to the distribution of the density fluctuation upstream, the fluctuation profiles in the curved ramp are similar; however, a rapid increase is observed in the outer part, significantly faster than that in the near-wall region. In contrast, the velocity fluctuation in the near-wall region is relatively unaffected, and the fluctuation intensities for $0.25 < y^*/\delta < 0.50$ exhibit an approximately threefold increase compared to the value upstream. The simulation results suggest that the surface curvature significantly affects the turbulent fluctuation in the outer region of the boundary layer.

Figure 13 shows the computed anisotropy invariant maps at the selected streamwise locations. This map comprises the second and third invariants of the Reynolds stress anisotropy

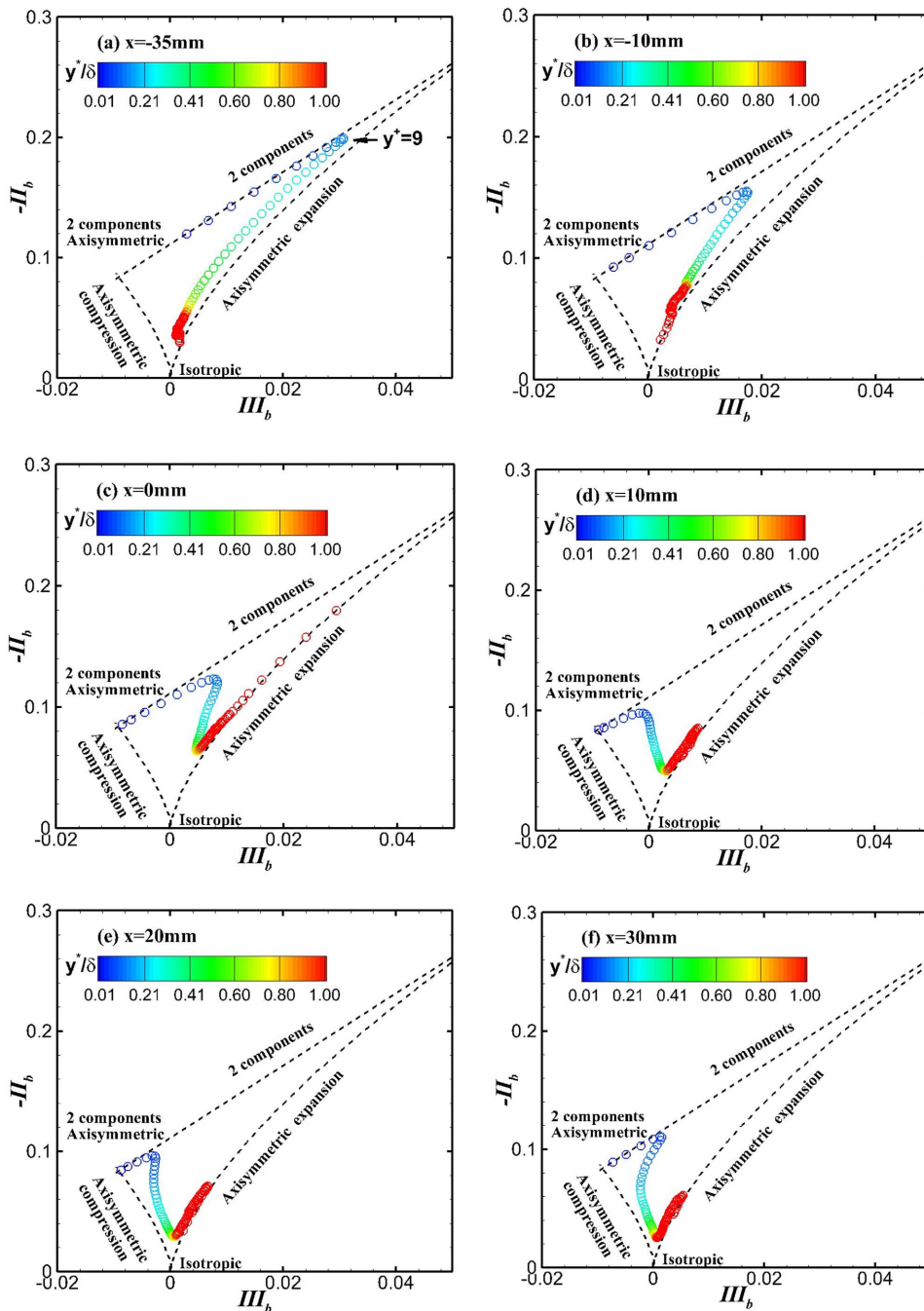


FIG. 13. Anisotropy invariant maps at selected streamwise locations along the curved compression ramp. The colored map denotes the normal distance (y^*/δ) from the wall.

tensor (b_{ij}), which are defined as follows:³¹

$$b_{ij} = \frac{\langle \rho u_i'' u_j'' \rangle}{2 \langle \rho \rangle \langle k \rangle} - \frac{1}{3} \delta_{ij}, \quad \Pi_b = b_{ij} b_{ji}, \quad \text{and} \quad \text{III}_b = b_{ij} b_{jk} b_{ki}. \quad (7)$$

Lumley³² demonstrated that the evolution of the turbulence state through the curved ramp could be obtained by investigating the anisotropy invariant map. Figure 13(a) shows the turbulence states of the incoming turbulent boundary layer. It is clear that the near-wall region is characteristic of a two-component turbulence and the outer region is represented by isotropic turbulence. Moreover, the maximum anisotropy occurred at $y^+ \approx 9$, which falls approximately in the buffer layer. The results are consistent with that obtained for a canonical flat-plate turbulent boundary layer.³³ Figures 13(b)–13(d) show the change in the turbulence state throughout the curved ramp. From the streamwise positions of $x = -10$ mm to $x = 10$ mm, the turbulence in the near-wall and outer regions evolves differently. In particular, the two-component axisymmetric turbulence is gradually attained in the proximity of the wall because of the blocking effect.³³ Furthermore, the maximum anisotropy is reduced in the near-wall region and the turbulence state approaches axisymmetric compression. These behaviors are observed in the DNS conducted by Grilli *et al.*³⁴ However, in the outer region, the anisotropy increases and subsequently decreases toward the isotropic turbulence along the line corresponding to the axisymmetric expansion. Downstream of the curved region in the compression ramp, the anisotropy increases in the near-wall region; however, the change in the turbulence state in the outer region is negligible, as shown in Figs. 13(e) and 13(f). This indicates that there exists a faster reversal tendency in the near-wall region than that in the outer part. Based on the comparison with the results shown in Fig. 13(a), the disturbed turbulent boundary layer does not fully recover to its equilibrium state.

To study the near-wall asymptotic behavior, the distributions of the turbulent kinetic energy (TKE) at various locations are plotted, as shown in Fig. 14. For the incompressible

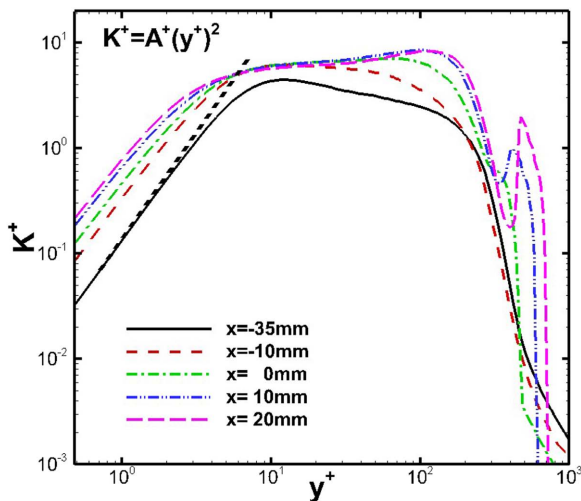


FIG. 14. Distribution of the turbulent kinetic energy at various streamwise locations.

boundary layer,^{35,36} the TKE within the near-wall region obeys the following asymptotic behavior:

$$K^+ \approx A^+(y^+)^2, \quad (8)$$

where A^+ is a constant. Figure 14 shows that the viscous sub-layer of the upstream supersonic turbulent boundary layer satisfies the above equation for $A^+ = 0.135$, which is somewhat smaller than the value obtained in the DNS conducted by Pirozzoli *et al.* ($A^+ = 0.2035$).²³ This is because of the difference in the inflow conditions. In addition, the peak value of the TKE is approximately 4.42 at $y^+ = 12.2$, which is in good agreement with that obtained in previous compressible flows. Although the TKEs in the near-wall and outer regions are significantly enhanced along the curved ramp, the evolving process is significantly different. It is clear that the TKE in the near-wall region not only increases linearly but also obeys the asymptotic behavior with a larger constant A^+ than that of the upstream compressible turbulent flat-plate boundary layer. The TKE in the outer region increases dramatically and reaches a peak value for $10 \text{ mm} < x < 20 \text{ mm}$. This suggests that the curvature effect has different underlying mechanisms on the inner and outer regions of the turbulent boundary layer.

Figure 15 shows the isocontour lines of the TKE and Reynolds shear stress in the curved ramp. The TKE is amplified across the curved ramp. It is clear that the turbulence reaches a maximum value in the downstream region of the curved ramp ($10 \text{ mm} < x < 20 \text{ mm}$). This is different from that obtained in previous DNS results of the compression ramp¹⁷ with similar inflow conditions and total turning angle, where the peak value of the TKE is observed at the separated shear layer. This discrepancy could be related to the weaker adverse pressure gradient, where the mean flow in the curved

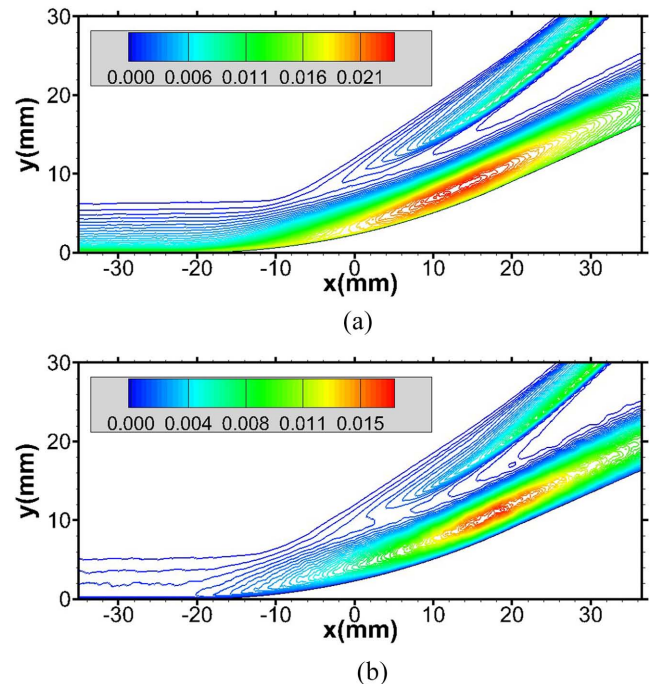


FIG. 15. (a) Isocontour lines of the turbulent kinetic energy and (b) Reynolds shear stress in the curved ramp.

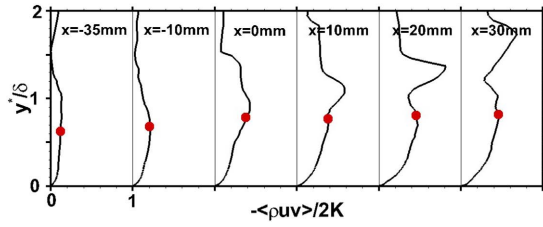


FIG. 16. Streamwise distribution of the structure parameter in the curved ramp.

ramp is attached statistically. However, as shown in Fig. 15(b), the effect of the concave curvature on the distribution of the Reynolds shear stress is negligible. Consistent with the recent simulation results of the compression ramp,¹⁷ the peak region of the Reynolds shear stress is still observed at similar streamwise locations (at approximately $x = 20$ mm) with comparable values.

The structure parameter, which is defined as the ratio of the shear stress to the trace of the Reynolds stress tensor, is plotted in Fig. 16, where the red dots denote the wall-normal location of the maximum structure parameter in the turbulent boundary layer. This change can be used to illustrate the amplification mechanism for the normal and shear components of the Reynolds stress tensor. In agreement with previous experimental and numerical findings, the concave curvature has different effects on the amplification mechanism. Upstream of the curved region, a nearly constant peak value is obtained at approximately 0.15 toward the edge of the boundary layer. This is similar to the DNS data reported by Adams.¹⁴ Subsequently, the structure parameter is found to increase dramatically from 0.2 at $x = -10$ mm to 0.38 at $x = 10$ mm throughout the curved region. Downstream of the curved ramp, the same trend is observed inside the boundary layer. However, a secondary peak is visible outside the boundary layer, corresponding to the shock wave.

To further study the concave curvature effect on the transport mechanism of the TKE, various budget terms in the TKE transport equation are discussed. The transport equation of the TKE in the compressible form is given as follow:¹⁵

$$\frac{\partial}{\partial t}(\bar{\rho}k) = C + P + T + V + \varepsilon + \Pi + M, \quad (9)$$

where C , P , T , V , ε , Π , and M are the advection, production, turbulent transport, viscous diffusion, viscous dissipation, pressure dilation, and mass diffusion terms, respectively. The explicit expressions of these terms are given as follows:¹⁵

$$\begin{aligned} C &= -\partial(\bar{u}_j \bar{\rho}k)/\partial x_j, & P &= -\overline{\rho u'_i u'_j} \partial \bar{u}_i / \partial x_j, \\ T &= -\partial(1/2 \overline{\rho u'_i u'_i u'_j} + \overline{p' u'_j})/\partial x_j, \\ V &= \partial \overline{\sigma'_{ij} u'_i} / \partial x_j, \\ \varepsilon &= \overline{\sigma'_{ij} \partial u'_i / \partial x_j}, \\ \Pi &= \overline{p' \partial u'_i / \partial x_i}, \\ M &= \bar{u}'_i (\partial \bar{\sigma}_{ij} / \partial x_j - \partial \bar{p} / \partial x_i), \end{aligned} \quad (10)$$

where the over bar and tilde variables denote the Reynolds-averaged and Favre-averaged values, respectively. The prime

and double prime variables correspond to the fluctuations. Figure 17 shows the profiles of the significant terms in the TKE transport equation at $x = -35$ mm and $x = 0$ mm, respectively. As shown in Fig. 17(a), the results are characteristic of a zero-pressure gradient turbulent flat-plate boundary layer. The production term is balanced with the turbulent transport term for a major portion of the boundary layer, suggesting that the TKE is transported from the far-from-wall region to the near-wall region by the turbulent transport. In the near-wall region, the viscous dissipation term largely balances with the viscous diffusion term, indicating that the turbulence is dissipated in the near-wall region because of the viscous effect. It is clear that the sum of all the terms exhibits an overall balance. This indicates that the boundary layer is in an equilibrium state. In Fig. 17(b), the magnitude of the corresponding terms increases significantly in region II. Moreover, the behavior of the turbulent boundary layer in the curved ramp is different. The peak value of the turbulent production term in the TKE equation is

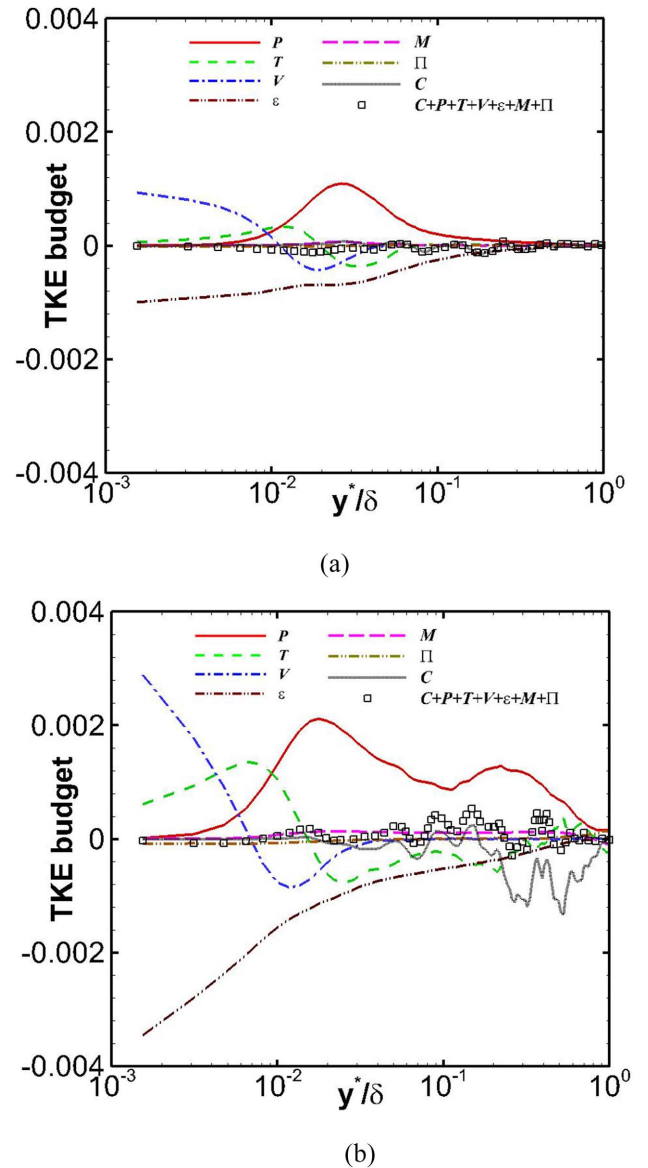


FIG. 17. Budget of the turbulent kinetic energy: (a) $x = -35$ mm, region I, and (b) $x = 0$ mm, region II.

attained in the outer region of the boundary layer. This is due to the interaction with the shock wave. Furthermore, compared with the upstream turbulent boundary layer, the advection term becomes significant at $y^*/\delta > 0.1$, as shown in Fig. 17(b). It is suggested that the TKE budget in the outer part of the boundary layer in the corner region is dominated by the production and advection term.

D. Görtler-like vortex

When the flow develops on the concave curvatures, the so-called Taylor–Görtler vortex, which is due to a combined interaction between the centrifugal instability, pressure gradient and viscosity, has been the subject of many numerical and experimental investigations. As reported by Loginov *et al.*,³⁷ the spanwise inhomogeneity of the mean skin-friction coefficient is associated with the Görtler-like vortices and the structures are supposed to be steady. However, in the DNS analysis of the compression ramp, Priebe *et al.*³⁸ found that the Görtler-like vortices observed in the interaction are unsteady. It should be noted that the characteristics of the Görtler vortex have not been fully understood.

Figure 18(a) shows the contours of the mean skin-friction coefficient along the curved ramp. The start and end locations of the curved region are indicated by vertical black lines. Figures 18(b) and 18(c) show the spanwise variation in the skin-friction at two streamwise locations, $x = -5$ mm and $x = 30$ mm, respectively. In the curved region and the downstream of this region, the results show a significant variation in the spanwise direction with the characteristic of a streak structure. A similar trend was observed in previous simulations conducted by Grilli *et al.*³⁴ and Loginov *et al.*³⁷ It was proposed that the regions of the low and high skin-friction are due to the up and down wash effects of the steady Görtler-like vortices.^{34,37}

For the supersonic turbulent boundary layer subjected to a concave surface curvature, a stability criterion, namely, Görtler number (G_T), was proposed to assess the Görtler instability. It is similar to that of a laminar and incompressible flow,³⁹ which is defined as follows:

$$G_T = \frac{\theta}{0.018\delta^*} \sqrt{\frac{\theta}{R}}, \quad (11)$$

$$R = \frac{1}{\kappa}, \kappa = \frac{\left[u^2 \frac{\partial v}{\partial x} - v^2 \frac{\partial u}{\partial y} + uv \left(\frac{\partial v}{\partial y} - \frac{\partial u}{\partial x} \right) \right]}{(u^2 + v^2)^{3/2}}.$$

Here, θ and δ^* denote the boundary layer momentum and displacement thickness, respectively. The variable R is given by the curvature radius of the flow throughout the curved ramp. Note that the Görtler number in this simulation is computed using the time and spanwise averaged flow-field. Figure 19(a) shows the contours of the Görtler number. The black solid contours denote the critical value, which is approximately 0.6.³⁹ The values are high along the main shock and in the boundary layer in the curved region for -20 mm $< x < 20$ mm. Figure 19(b) shows the three streamlines, indicated by white solid lines, through the boundary layer. Generally, the trends in the different streamlines are similar. In the incoming boundary layer, the Görtler number is very small and, subsequently, increases beyond the critical value when the flow enters the curved region. Along the streamlines, the value increases through the entire curved region. Subsequently, it decreases dramatically below 0.6 in the downstream region of the curved ramp.

To further verify the occurrence of streamwise vortices in the curved ramp, the isosurface of the instantaneous streamwise vorticity is plotted, as shown in Fig. 20. The positive and negative values are indicated using red and blue, respectively.

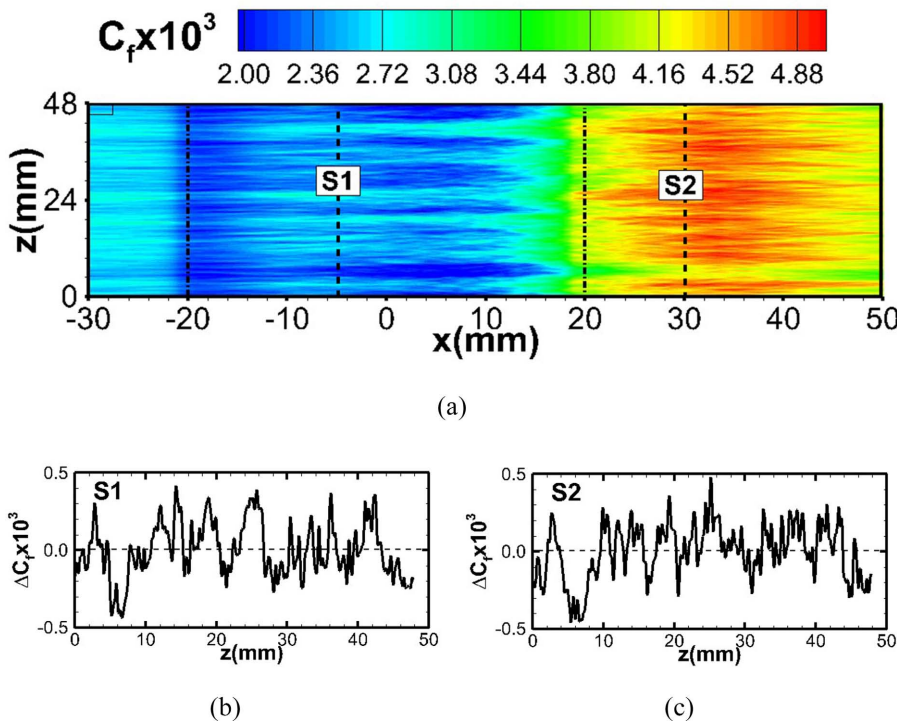


FIG. 18. (a) Contours of the mean skin-friction on the curved ramp. The line plots of the mean skin-friction as a function of the spanwise position are taken at locations S1 (b) and S2 (c), respectively.

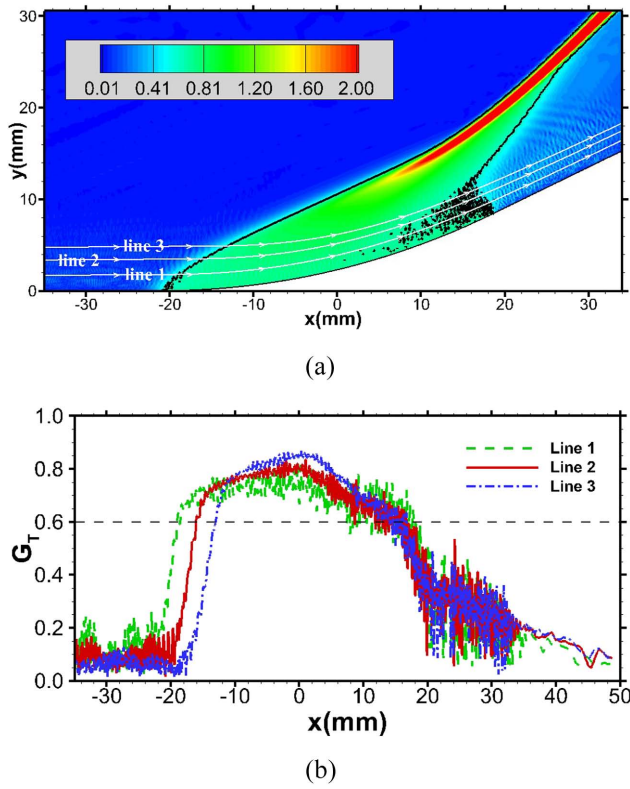


FIG. 19. (a) Contours of the Görtler number (G_T) and (b) streamwise distribution of the turbulent Görtler number along the streamlines. The black solid lines denote the critical value with 0.6. The normal locations of the streamlines are indicated using white solid lines.

As expected, the streamwise vortex in the spanwise direction is characteristic of alternating positive and negative regions, consistent with the pattern of Görtler-like vortices. Another notable characteristic is that the spatial scale of the above positive and negative regions increases rapidly as the boundary layer develops along the curvature surface, particularly in the downstream region of the curved ramp. This suggests that the concave curvature enhances the streamwise vortex structure. In particular, the distribution of the streamwise vorticity is characterized by intermittency. For a deeper understanding, Figs. 21 and 22 show the contours of the streamwise vorticity in the spanwise and wall-normal planes selected at

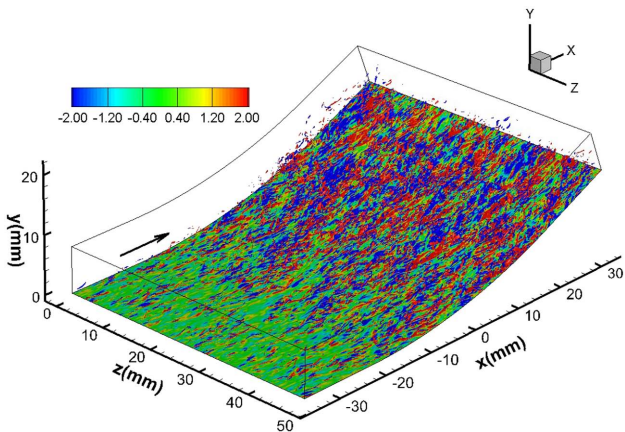


FIG. 20. Isosurface of the instantaneous streamwise vorticity.

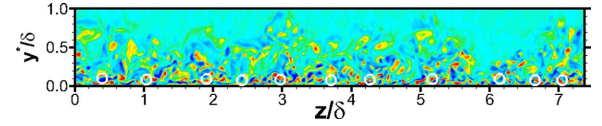


FIG. 21. Contour plot of the instantaneous streamwise vorticity in the spanwise/wall-normal plane at $x = -20$ mm.

two streamwise locations, respectively. The data, shown in Fig. 21, were obtained at the incoming turbulent boundary layer. As expected, the streamwise vortices, indicated using the white circles, are concentrated in the near-wall region. This is because the near-wall region of the compressible flat-plate turbulent boundary layer is characterized by the streamwise aligned legs of the hairpin vortices. For a more direct view of the curvature effect on these vortices, Fig. 22 shows the results at $x = 30$ mm. Apparently, in contrast with the incoming boundary layer, the spanwise structure is dominated by the large-scale streamwise vortex packets, which are centered in the outer region of the boundary layer at $y^*/\delta = 0.5$. In addition, to better depict the unsteadiness of the vortex structure, Fig. 22 shows the two different instantaneous flow-fields. Clearly, the vortex packets, labeled as A–D, undergo a significant variation. Based on the above analysis, the existence of unsteady Görtler-like vortices in the curved compression ramp is confirmed.

E. Dynamic mode decomposition

The dynamic mode decomposition (DMD), proposed by Schmid,⁴⁰ is a relatively new data-driven spectral analysis technique, which is based on the Koopmans analysis of a non-linear dynamic system. The modal analysis helps in understanding the dynamic processes associated with characteristic frequencies. Recently, Jovanovic *et al.*⁴¹ developed a sparsity promoting dynamic mode decomposition (namely, DMDSP) to achieve a trade-off between the number of extracted dynamic modes and the accuracy of reconstruction. According to Jovanovic *et al.*,⁴¹ the DMDSP algorithm is briefly outlined as follows:

- (a) Two snapshot matrices, namely, ψ_0 and ψ_1 , are used as input. The matrices contain the numerical dataset sampled at a constant time step and are assembled as follows:

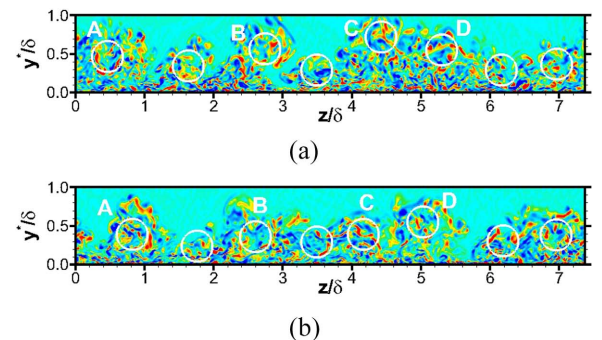


FIG. 22. Contour plots of the instantaneous streamwise vorticity in the spanwise/wall-normal plane at $x = 30$ mm. (a) $t = 960$ and (b) $t = 1800$.

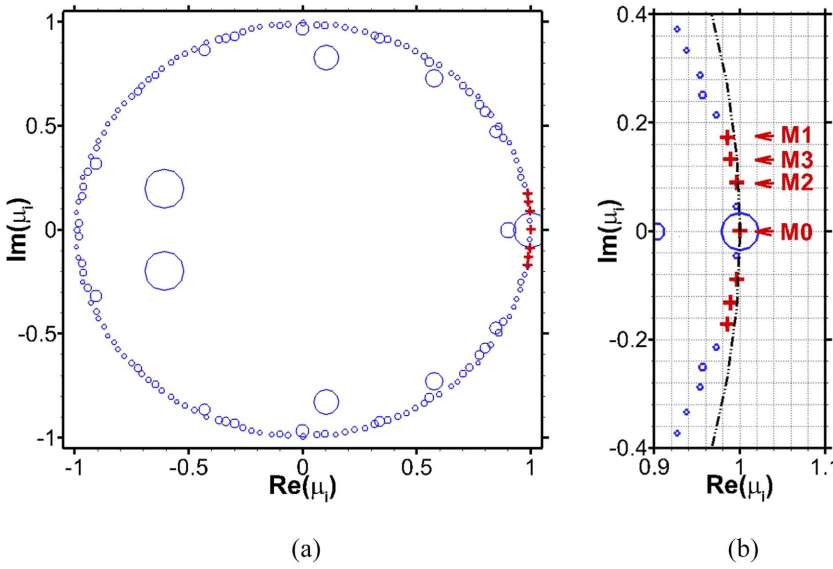


FIG. 23. Eigenvalues obtained using the DMD algorithm (circle) and the DMDSP algorithm (cross). The dashed curve denotes the unit circle.

$$\psi_0 = [v_0, v_2, \dots, v_{N-1}] \text{ and } \psi_1 = [v_1, v_2, \dots, v_N], \quad (12)$$

where v is the flow variable and the subscript denotes the index of the flow-field snapshot. The objective of the DMD is to obtain a low-order representation of the mapping matrix A between the two snapshot matrices.

- (b) An optimal representation of the mapping matrix A is given as follows:

$$F_{DMD} = U^* \psi_1 V \Sigma^{-1}. \quad (13)$$

Here, U , V , and Σ are obtained by an economy-size singular value decomposition of the snapshot matrix ψ_0 . The flow-field reconstruction is obtained as follows:

$$\underbrace{\begin{bmatrix} \psi_0 \\ v_0 v_1 \dots v_{N-1} \end{bmatrix}}_{\psi_0} \approx \underbrace{\begin{bmatrix} \phi \\ \phi_1 \phi_2 \dots \phi_{N-1} \end{bmatrix}}_{\phi} \begin{bmatrix} D_\alpha \\ \alpha_1 \\ \alpha_2 \\ \vdots \\ \alpha_r \end{bmatrix} \begin{bmatrix} V_{and} \\ 1\mu_1 \dots \mu_1^{N-1} \\ 1\mu_2 \dots \mu_2^{N-1} \\ \vdots \\ 1\mu_r \dots \mu_r^{N-1} \end{bmatrix}.$$

The matrix of the dynamic modes ϕ is computed as $\phi_i = U y_i$, where y_i is the eigenvector of F_{DMD} . The diagonal matrix D_α is obtained using the amplitude vector α_i . The Vandermonde matrix V_{and} , which represents the temporal evolution of the dynamic modes, is formed by the eigenvalues μ_i of F_{DMD} .

- (c) To balance the number of extracted modes and the error of reconstruction, the objective function with a punishment term is constructed as follows:

$$\underset{\alpha}{\text{minimize}} \|\Sigma V^* - \Lambda D_\alpha V_{and}\|_F^2 + \gamma \sum_{i=1}^r |\alpha_i|, \quad (14)$$

where Λ denotes the matrix holding the eigenvectors and $\|\cdot\|_F^2$ denotes the Frobenius norm. The user-defined γ is used to emphasize the dynamically significant modes. A sparsity structure of the amplitude vector associated with the most relevant modes is obtained by solving the optimization problem using alternating direction method of

the multipliers. A complete description of this method can be found in the study conducted by Jovanovic *et al.*⁴¹

In this section, the streamwise velocity field is quantitatively analyzed using the DMDSP method to extract the characteristic dynamic modes from the simulation results. The modal analysis is conducted using 160 snapshots of the spanwise and wall-normal planes at the streamwise location ($x = 30$ mm), and the time spacing of the inter-snapshot is approximately $1.23\delta/U_\infty$. As shown in Fig. 18, the selected location is at the region of high and low skin frictions, labeled as **S2**.

Figure 23 shows the distribution of the eigenvalues, where the symbol size denotes the amplitude of the mode ($|\alpha_i|$). It is clear that the obtained modes are symmetric about the real axis because of the real-valued simulation data. Moreover, the modes are present inside or along the unit circle, suggesting that these modes are saturated. In addition, the modes M0–M3 obtained using the DMDSP method are labeled with red crosses in Fig. 23. Compared to the total snapshots, the performance loss of the reconstruction with the four modes is approximately 16%. The four modes are close to the unit circle. Table II lists the frequency (fU_∞/δ) and growth rate ($|\lambda_i|$) of the four modes, computed using logarithmic transformation.⁴⁰ The mode M0 with the largest amplitude and the lowest growth rate is related to the mean-averaged flow. The frequencies of the dynamic modes M1–M3 are 0.0115, 0.0172, and 0.0223, respectively. In comparison with the characteristic frequency of the turbulent boundary layer (approximately 1.0), these modes are characteristic of low frequency. Figure 24 shows the dependency of the amplitude of the modes

TABLE II. Four modes obtained using the DMDSP method.

Mode name	$ \alpha_i $	fU_∞/δ	$ \lambda_i $
M0	194.4747	0.0000	1.55×10^{-5}
M1	2.1335	0.0115	2.17×10^{-4}
M2	3.0345	0.0172	1.65×10^{-3}
M3	2.3380	0.0223	2.84×10^{-4}

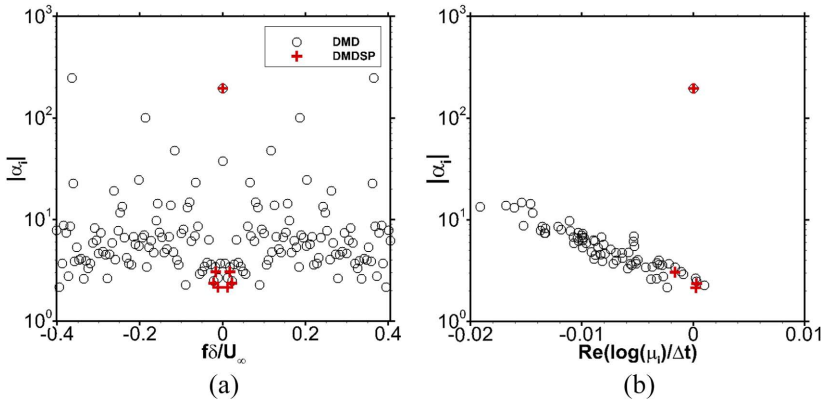


FIG. 24. (a) Effects of the mode amplitude on (a) the frequency and (b) the growth rate of the dynamic modes. Circle: DMD; Cross: DMDSP.

on the frequency and growth rate. Based on the findings of Jovanovic *et al.*,⁴¹ although the amplitude of the three dynamic modes are small, the decay rates are much smaller than that of the modes with higher amplitudes. Therefore, the latter is strongly damped and has a strong influence only during the early stage of the evolution; however, the former plays a major role during the entire process. Hence, the low-frequency modes are dynamically relevant.

To depict the spatial structure, Fig. 25 shows the real part of the modes M0–M3. Generally, the structures of the mean and dynamic modes are different. It is apparent that the mode M0 is consistent with the time-averaged streamwise velocity flow-field. The dynamic modes M1–M3 clearly exhibit a relatively similar spatial structure. They are regularly distributed in the spanwise direction, with an alternating velocity fluctuation that

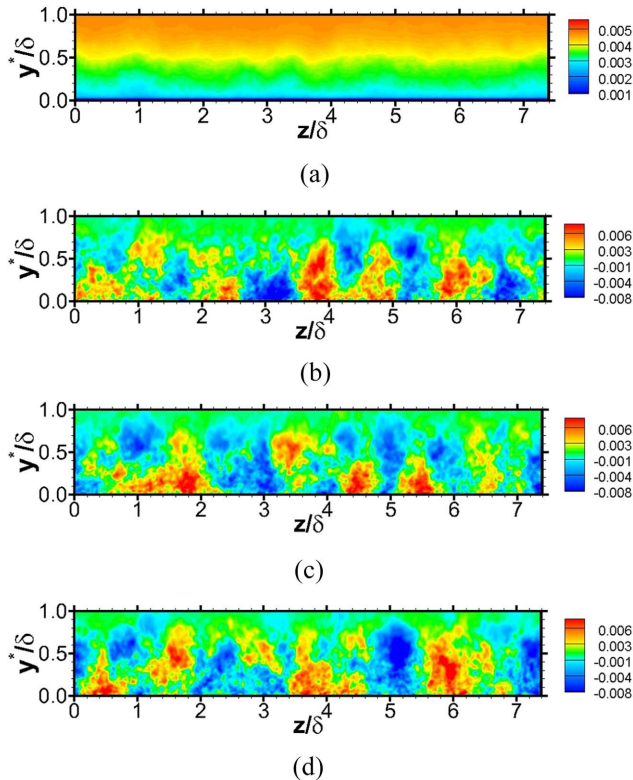


FIG. 25. Real part of the modes from streamwise velocity data: (a) M0, (b) M1, (c) M2, and (d) M3.

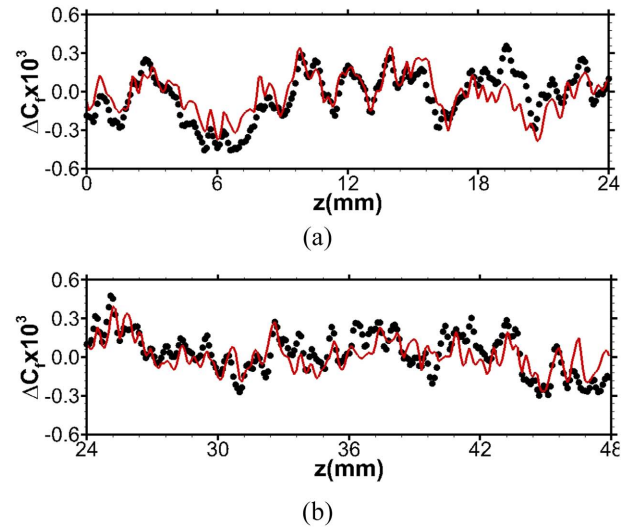


FIG. 26. Wall skin friction coefficient as a function of the spanwise position at $x = 30$ mm. (a) $0 \text{ mm} < z < 24 \text{ mm}$ and (b) $24 \text{ mm} < z < 48 \text{ mm}$. Symbol: DNS; line: DMD modes from DNS.

appears in the boundary layer. It is interesting to note that the dynamic modes have a strong relationship with the Görtler-like vortices. Furthermore, we can clearly see that the spatial scales of the three modes are similar, which is approximately one boundary layer thickness. Figure 26 shows the comparison of the wall skin-friction coefficient reconstructed using the above four modes with the exact DNS data. The agreement is satisfactory in general. The reconstructed results show a good approximation of the data from the DNS, further supporting the above conclusion that the four modes obtained using the DMDSP method provide an optimal low-order representation of the original DNS data.

IV. CONCLUSIONS

A numerical investigation using the DNS is performed to study the response of the supersonic turbulent boundary layer subjected to a curved compression ramp with a turning angle of 24° . Various mechanisms associated with the complex curved flow are analyzed systematically, including the mean and instantaneous flow properties, turbulent boundary layer statistics, and characteristic of the Görtler-like vortices.

As expected, the instantaneous density gradient analysis reveals that a fan of the compression wave occurs at the foot of the shock wave because of the weak adverse pressure gradient induced by the concave curvature. Because of the enforcing effect, the outer region of the boundary layer downstream of the curved ramp is characterized by organized large-scale hairpin vortex packets. The mean and instantaneous wall skin-friction coefficients indicate that the mean flow is attached statistically; however, the instantaneous flow field is close to the incipient detachment state, exhibiting strong unsteadiness and intermittency. The evolution of the turbulent boundary layer is studied in terms of the mean velocity profile, fluctuation intensity, anisotropy of the Reynolds stress, and TKE. Consistent with previous experimental observations, the logarithmic region of the velocity profiles in the curved region is relatively unaffected, exhibiting a good agreement with the logarithmic law. The turbulence intensity is amplified dramatically, up to thrice that of the upstream value. The variation in the turbulent state in the inner and outer regions of the boundary layer is comparatively studied using anisotropy invariant maps. The effects on the turbulence state in the above two layers are different. In the inner layer, the anisotropy reduces and the turbulence state approaches the axisymmetric compression. Anisotropy in the outer layer increases and subsequently decreases toward isotropic turbulence along the line corresponding to the axisymmetric expansion. The balance of TKE budget in the curved ramp is still obtained, however, with the increase in the wall-normal distance, the magnitude of the advection term in TKE equation increases significantly, particularly in the outer region of the boundary layer. The balance is dominated by the strong turbulent production and advection terms.

The existence of the Görtler-like vortices is visualized by the alternating positive and negative streamwise vorticities. Moreover, compared to the upstream boundary layer, the Görtler-like vortex structure is significantly enhanced and centered in the outer part of the boundary layer. The results further confirm the hypothesis that the unsteady Görtler-like roll cells might exist in the curved flow.

In addition, the DMD analysis of the streamwise velocity is performed to determine the dynamically significant modes. The skin-friction coefficient reconstructed using the extracted four modes is in good agreement with the DNS results, suggesting that the reconstructed flow field with a performance loss of 16% provides an optimal representation of the DNS data. The spatial structures of the dominated low-frequency dynamic modes are consistent with the spanwise distribution of Görtler-like vortices.

ACKNOWLEDGMENTS

This work is based on the research sponsored by the National Key Research and Development Program of China (2016YFA0401200) and the National Natural Science Foundation of China (Grant Nos. 91441103, 11372330, and 11472278). The authors would like to thank the Supercomputing Center of the Chinese Academy of Sciences (SCCA) and the Tianjin Supercomputer Center (TSC) for providing computer time.

- ¹A. J. Smits and D. H. Wood, "The response of turbulent boundary layer to sudden perturbations," *Annu. Rev. Fluid Mech.* **17**, 321 (1985).
- ²E. F. Spina, A. J. Smits, and S. K. Robinson, "The physics of supersonic turbulent boundary layers," *Annu. Rev. Fluid Mech.* **26**, 287 (1994).
- ³P. Bradshaw, "The effect of mean compression or dilatation on the turbulence structure of supersonic boundary layers," *J. Fluid Mech.* **63**, 449–464 (1974).
- ⁴S. Tandiono, S. H. Winoto, and D. A. Shah, "On the linear and nonlinear development of Görtler vortices," *Phys. Fluids* **20**, 094103 (2008).
- ⁵J. D. Swearingen and R. F. Blackwelder, "The growth and breakdown of streamwise vortices in the presence of a wall," *J. Fluid Mech.* **182**, 255 (1987).
- ⁶M. Jayaram, M. W. Taylor, and A. J. Smits, "The response of a compressible turbulent boundary layer to short regions of concave surface curvature," *J. Fluid Mech.* **175**, 343 (1987).
- ⁷J. F. Donovan, E. F. Spina, and A. J. Smits, "The structure of a supersonic turbulent boundary layer subjected to concave surface curvature," *J. Fluid Mech.* **259**, 1 (1994).
- ⁸Q. C. Wang and Z. G. Wang, "Structural characteristics of the supersonic turbulent boundary layer subjected to concave curvature," *Appl. Phys. Lett.* **108**, 114102 (2016).
- ⁹Q. C. Wang, Z. G. Wang, and Y. X. Zhao, "An experimental investigation of the supersonic turbulent boundary layer subjected to concave curvature," *Phys. Fluids* **28**, 096104 (2016).
- ¹⁰P. H. Hoffmann, K. C. Muck, and P. Bradshaw, "The effect of concave surface curvature on turbulent boundary layers," *J. Fluid Mech.* **161**, 371 (1985).
- ¹¹W. B. Sturek and J. E. Danberg, "Supersonic turbulent boundary layer in adverse pressure gradient. Part I: The experiment," *AIAA J.* **10**, 475 (1972).
- ¹²A. J. Laderman, "Adverse pressure gradient effects on supersonic boundary layer turbulence," *AIAA J.* **18**, 1186 (1980).
- ¹³P. Moin and K. Mahesh, "Direct numerical simulation: A tool in turbulence research," *Annu. Rev. Fluid Mech.* **30**, 539–578 (1998).
- ¹⁴N. A. Adams, "Direct simulation of the turbulent boundary layer along a compression ramp at $M = 3$ and $Re_\theta = 1685$," *J. Fluid Mech.* **420**, 47–83 (2000).
- ¹⁵X. L. Li, D. X. Fu and Y. W. Ma, "Direct numerical simulation of shock/turbulent boundary layer interaction in a supersonic compression ramp," *Sci. China: Phys., Mech. Astron.* **53**, 1651 (2010).
- ¹⁶F. L. Tong, Z. G. Tang, C. P. Yu, X. K. Zhu, and X. L. Li, "Numerical analysis of shock wave and supersonic turbulent boundary layer interaction between adiabatic and cold walls," *J. Turbul.* **18**, 569–588 (2017).
- ¹⁷M. Wu and M. P. Martin, "Direct numerical simulation of supersonic turbulent boundary layer over a compression ramp," *AIAA J.* **45**, 879 (2007).
- ¹⁸P. Booky, C. Wyckham, and A. Smits, "New experimental data of STBLI at DNS/LES accessible Reynolds numbers," AIAA paper 2005-309, 2005.
- ¹⁹S. Pirozzoli, "Numerical methods for high-speed flows," *Annu. Rev. Fluid Mech.* **43**, 163–194 (2011).
- ²⁰M. P. Martin, E. M. Taylor, M. Wu, and V. G. Weirs, "A bandwidth-optimized WENO scheme for the effective direct numerical simulation of compressible turbulence," *J. Comput. Phys.* **220**, 270 (2006).
- ²¹S. Gottlieb and C. W. Shu, "Total variation diminishing Runge-Kutta schemes," *Math. Comput. Am. Math. Soc.* **67**, 73–85 (1998).
- ²²X. H. Wu, "Inflow turbulence generation methods," *Annu. Rev. Fluid Mech.* **49**, 23–49 (2017).
- ²³S. Pirozzoli, F. Grasso, and T. B. Gatski, "Direct numerical simulation and analysis of a spatially evolving supersonic turbulent boundary layer at $M = 2.25$," *Phys. Fluids* **16**, 530 (2004).
- ²⁴S. Pirozzoli and M. Bernardini, "Turbulence in supersonic boundary layers at moderate Reynolds numbers," *J. Fluid Mech.* **688**, 120–168 (2011).
- ²⁵X. Wu and P. Moin, "Direct numerical simulation of turbulence in a nominally zero-pressure-gradient flat-plate boundary layer," *J. Fluid Mech.* **630**, 5 (2009).
- ²⁶L. P. Erm and P. N. Joubert, "Low Reynolds number turbulent boundary layers," *J. Fluid Mech.* **230**, 1–44 (1991).
- ²⁷P. R. Spalart, "Direct numerical simulation of a turbulent boundary layer up to $Re_\theta = 1410$," *J. Fluid Mech.* **187**, 61–98 (1988).
- ²⁸J. Jeong and F. Hussain, "On the identification of a vortex," *J. Fluid Mech.* **285**, 69 (1995).
- ²⁹F. M. White, *Viscous Fluid Flow* (McGraw-Hill, 1974).
- ³⁰R. L. Simpson, "Turbulent boundary layer separation," *Annu. Rev. Fluid Mech.* **21**, 205 (1989).

- ³¹S. B. Pope, *Turbulent Flows* (Cambridge University Press, 2000).
- ³²J. L. Lumley, "Computational modeling of turbulent flows," *Adv. Appl. Mech.* **18**, 123 (1978).
- ³³S. Pirozzoli, M. Bernardini, and F. Grasso, "Direct numerical simulation of transonic shock/boundary layer interaction under conditions of incipient separation," *J. Fluid Mech.* **657**, 361–393 (2010).
- ³⁴M. Grilli, S. Hickel, and N. A. Adams, "Large-eddy simulation of a supersonic turbulent boundary layer over compression-expansion ramp," *Int. J. Heat Fluid Flow* **42**, 79–93 (2013).
- ³⁵V. C. Patel, W. Rodi, and G. Scheuerer, "Turbulence models for near-wall and low Reynolds number flows: A reviews," *AIAA J.* **23**, 1308–1319 (1985).
- ³⁶C. G. Speziale, R. Abid, and E. C. Anderson, "Critical evaluation of two-equation models for near-wall turbulence," *AIAA J.* **30**, 324–331 (1992).
- ³⁷M. S. Loginov, N. A. Adams, and A. A. Zheltovodov, "Large eddy simulation of shock wave/turbulent boundary layer interaction," *J. Fluid Mech.* **565**, 135–169 (2006).
- ³⁸S. Priebe, J. H. Tu, C. W. Rowley, and M. P. Martin, "Low-frequency dynamics in a shock-induced separated flow," *J. Fluid Mech.* **807**, 441–477 (2016).
- ³⁹I. Tani, "Production of longitudinal vortices in the boundary layer along a concave wall," *J. Geophys. Res.* **67**, 3075–3080, <https://doi.org/10.1029/jz067i008p03075> (1962).
- ⁴⁰P. J. Schmid, "Dynamic mode decomposition of numerical and experimental data," *J. Fluid Mech.* **656**, 5 (2010).
- ⁴¹M. R. Jovanovic, P. J. Schmid, and J. W. Nichols, "Sparsity promoting dynamic mode decomposition," *Phys. Fluids* **26**, 024103 (2014).